International Journal of Mechanical Sciences 98 (2015) 29–38

Contents lists available at ScienceDirect

International Journal of Mechanical Sciences

journal homepage: www.elsevier.com/locate/ijmecsci

The Yoffe-type moving tubular interface crack in a hollow composite cylinder with finite length

Pengpeng Shi [a,b], Xiaojing Zheng [a,b,*]

[a] School of Mechno-Electronic Engineering, Xidian University, Xi'an 710071, Shaanxi, PR China
[b] Key Laboratory of Mechanics on Disaster and Environment in Western China (Lanzhou University), the Ministry of Education, Lanzhou 730000, PR China

ARTICLE INFO

Article history:
Received 14 June 2014
Received in revised form
7 April 2015
Accepted 9 April 2015
Available online 18 April 2015

Keywords:
Composition cylinder
Yoffe-type moving crack
Tubular interface crack
Singular integral equation
Stress intensity factors

ABSTRACT

In this paper, the problem of a composite hollow cylinder with a constant-velocity Yoffe-type moving tubular interface crack is considered. For four frequently encountered constraint edges, i.e. free-free, clamped-clamped, free-clamped, or clamped-free edges, the mixed boundary value problem associated with a mode-III crack is reduced to a Cauchy kernel singular integral equation by applying the Fourier transform. Then, the numerical results of stress intensity factors (SIFs) are obtained by the Lobatto–Chebyshev quadrature technique from the singular integral equation. Numerical results of SIFs show that there exists a coupled effect of geometrical and physical parameters on the interfacial fracture behavior, which clearly relates to the selection of constraint edges. It is also observed that SIF increases as the crack moving velocity increases for the free–free, free–clamped, or clamped–free edges, and SIF is a decreasing function of the crack moving velocity for the clamped–clamped edge.

1. Introduction

Owing to the inherently high specific mechanical properties of the cylindrical composites, they are commonly used as primary structures in many applications such as aerospace, sport equipments, pressure vessels and automobile parts[1]. In such composites, the interface is significant for the mechanical loadings transmitting but meanwhile often has manufacturing defects, making the composites prone to damage. Therefore, interface analysis is important for the designs and evaluations of composite cylinder and has absorbed the attention of many researchers. Based on the complex variable method, the plane problem of a circular-arc crack in an infinite electrostrictive solid under remote electric fields is studied by Zheng and Gao[2]. Feng et al. [3] discussed the problem of multiple cracks on the arc-shaped interface of a semi-cylindrical magneto-electro-elastic layer bonded onto an orthotropic substrate which is formulated as a Cauchy singular integral equation by integrating the Green's function of an interfacial point dislocation. Fan et al. [4] carried out the stress analysis for a curved interfacial Zener–Stroh crack between a circular inclusion and an infinite matrix due to interface debonding in a composite. Based on the methods of variable separation and singular integral equation, Shi et al. [5] investigated the arc-shaped interfacial cracking problem in a hollow cylinder that consists of an inner orthotropic dielectric substrate and an outer functionally graded piezoelectric layer. Recently, Shi et al. [6] and Li and Shi [7] investigated two cyclic symmetric cracks problems on the arc-shaped interface in the functionally graded composition cylinder. Fan et al. [8] investigated the plastic zone size and the crack tip opening displacement for a curved interface crack between a circular inclusion and an infinite matrix. Their numerical examples show that both the crack debonding angle and the inclusion/matrix shear modulus ratio have significant influences on the normalized values of stress intensity factors, plastic zone size and the crack tip opening displacement. When a cylindrical interface is debonded, the angular sizes of interface crack in the models mentioned above are supposed to be only a part of the angular range; however, the crack may even occupy the whole angular range. Recently, the problem of a tubular interface crack in a bi-layered cylindrical composite of finite thickness under torsion is investigated by Li et al. [9].

Aforementioned studies which consider the fracture behavior of the cylindrical composites are mainly limited to static problems. Nevertheless, relatively few researches have been investigated in the arc-shaped interfacial dynamic crack problems in the cylindrical composites. Wang and Wang [10] investigated the scattering of SH waves by a rigid cylindrical inclusion partially debonded from its surrounding matrix by using the wave function expansion method and singular integral equation technique. Wang and Yu

* Corresponding author.
E-mail address: xjzheng@xidian.edu.cn (X. Zheng).

http://dx.doi.org/10.1016/j.ijmecsci.2015.04.009
0020-7403/

[11] obtained the scattered far field pattern and scattered cross section for scattering of SH waves by an arc-shaped crack between a cylindrical piezoelectric inclusion and matrix. Feng et al. [12] investigated the scattered field of SH waves by a magneto-electro-elastic cylindrical inclusion partially debonded from its surrounding magneto-electro-elastic material. Yoffe-type moving crack [13] means a crack that moves with a constant velocity while keeping its length unchanged. Consideration of Yoffe-type moving crack model could shed valuable insights into the effects of crack velocity, and could pave the way for the analysis of a more general dynamic fracture problem. So, Yoffe-type moving crack problems have also received some attention in recent years. Jin and Zhong [14] studied a moving mode-III crack in functionally graded piezoelectric materials. The crack surfaces are assumed to be permeable. Their results indicate that the stress intensity factor of moving crack depends only on the mechanical loading. The gradient parameter and the moving velocity of the crack do have significant influence on the dynamic stress intensity factor. Li and Weng [15] considered the problem of a functionally graded piezoelectric material with a constant-velocity Yoffe-type moving crack by using dual integral equations method and found that the electric field at the tip of the crack also exhibits the singularity of the inverse square root, along with the stress and electric displacement singularities. Kwon [16] studied a finite crack propagating at constant speed in a functionally graded piezoelectric material. Hu et al. [17] obtained the singular stress, electric fields and magnetic fields in a rectangular magnetoelectroelastic body containing a moving crack under longitudinal shear. Results show that the stress intensity factors are influenced by the material constants, the geometry size ratio and the velocity of the crack; in addition, the propagation of the crack possibly brings about branching phenomena. Yan and Jiang [18] provided a study of the problem of a propagating finite crack under in-plane loading in functionally graded piezoelectric materials. Shin and Lee [19] analyzed the dynamic propagation of an interface crack between two dissimilar functionally graded piezoelectric material layers under anti-plane shear by utilizing the integral transform method. Based on the Fourier transform and dual integral equation method, Hu et al. [20] considered a magnetoelectroelastic strip with a constant moving crack for the impermeable and permeable crack surface boundary conditions. This paper tries to reflect this edge affection on a composite hollow cylinder with a Yoffe-type moving tubular interface crack. Here the composite cylindrical edges are assumed either traction-free or clamped. With the Fourier integral transform, a mixed boundary value problem associated with the mode-III crack is reduced to a singular integral equation, from which the numerical results of the stress intensity factor are obtained by the Lobatto–Chebyshev quadrature technique. Numerical results of the stress intensity factors for geometrical and physical parameters are shown graphically for various combined constrain edges.

2. Basic equations and boundary conditions

Consider a composite hollow cylinder occupying $r_0 \le R \le r_2, 0 \le \vartheta < 2\pi, 0 \le Z \le L$, and with the length L, and the radii of the inner surface, interface and outer surface denoted by r_0, r_1, r_2, respectively. Hereafter, the subscripts/superscripts 1 and 2 refer to the quantities of the inner and outer cylinder, respectively. Here set up a cylindrical coordinate system (R, ϑ, Z) with the Z axis along the axis of the composite as shown in Fig. 1. A tubular crack is located at the interface between the inner and outer cylinder and parallel to the inner and outer surfaces of the composite cylinder. In other words, the crack is located at $R = r_1, a \le Z \le b, 0 \le \vartheta < 2\pi$. As in Yoffe's model, we assume that the crack moves along the Z-axis with a constant velocity v but the crack length $b-a$ remains unchanged as shown in Fig. 2.

2.1. Governing equations

The basic equation of a non-axisymmetric problem for a cylinder is shown here [21]. In the absence of body forces, the dynamic equilibrium equations are as follows in a circular coordinate system R, Z, ϑ

$$\begin{cases} \frac{\partial \sigma_R}{\partial R} + \frac{1}{R}\left(\frac{\partial \sigma_{R\vartheta}}{\partial \vartheta} + \sigma_R - \sigma_\vartheta\right) + \frac{\partial \sigma_{RZ}}{\partial Z} = \rho \frac{\partial^2 u_R}{\partial t^2} \\ \frac{\partial \sigma_{R\vartheta}}{\partial R} + \frac{1}{R}\left(\frac{\partial \sigma_\vartheta}{\partial \vartheta} + 2\sigma_{R\vartheta}\right) + \frac{\partial \sigma_{\vartheta Z}}{\partial Z} = \rho \frac{\partial^2 u_\vartheta}{\partial t^2} \\ \frac{\partial \sigma_{RZ}}{\partial R} + \frac{1}{R}\left(\frac{\partial \sigma_{\vartheta Z}}{\partial \vartheta} + \sigma_{RZ}\right) + \frac{\partial \sigma_Z}{\partial Z} = \rho \frac{\partial^2 u_Z}{\partial t^2} \end{cases} \quad (1)$$

where $\sigma_R, \sigma_\vartheta, \sigma_Z, \sigma_{\vartheta Z}, \sigma_{RZ}, \sigma_{R\vartheta}$ are mechanical stresses.

These strains are related to the displacement by Cauchy equations

$$\begin{cases} e_R = \frac{\partial u_R}{\partial R}; e_\vartheta = \frac{1}{R}\left(\frac{\partial u_\vartheta}{\partial \vartheta} + u_R\right); e_Z = \frac{\partial u_Z}{\partial Z}; \\ e_{R\vartheta} = \frac{1}{R}\left(\frac{\partial u_R}{\partial \vartheta} - u_\vartheta\right) + \frac{\partial u_\vartheta}{\partial R}; e_{RZ} = \frac{\partial u_Z}{\partial R} + \frac{\partial u_R}{\partial Z}; e_{Z\vartheta} = \frac{\partial u_\vartheta}{\partial Z} + \frac{1}{R}\frac{\partial u_Z}{\partial \vartheta}. \end{cases} \quad (2)$$

where u_R, u_ϑ, u_Z and $e_R, e_\vartheta, e_Z, e_{R\vartheta}, e_{RZ}, e_{Z\vartheta}$ are mechanical displacements and strains, respectively.

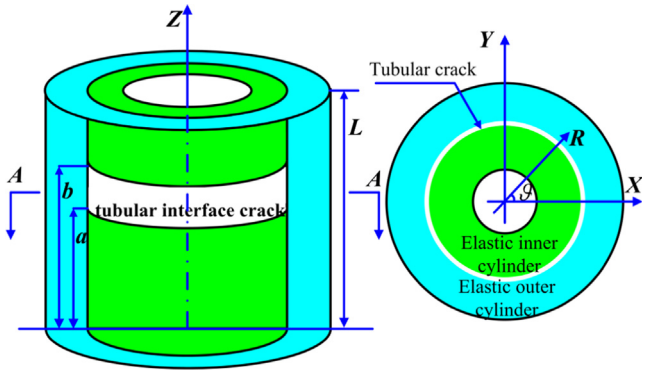

Fig. 1. A bi-layer cylinder with a tubular interface crack.

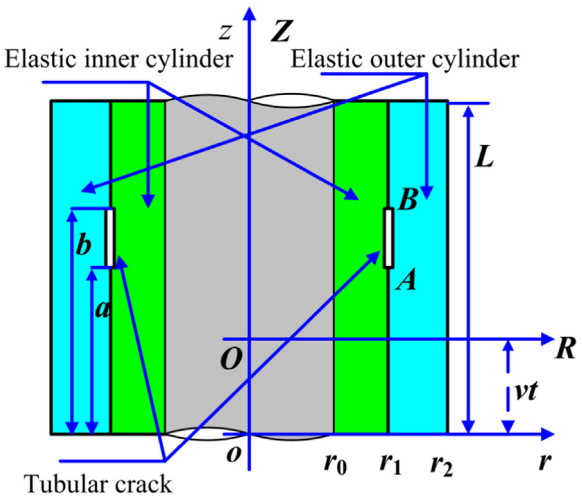

Fig. 2. The axial section of the bi-layer cylinder.

To close system (1)–(2), it is necessary to add the constitutive relations

$$\begin{cases} \sigma_R = \lambda_{11}e_R + \lambda_{12}e_\vartheta + \lambda_{13}e_Z \\ \sigma_\vartheta = \lambda_{12}e_R + \lambda_{11}e_\vartheta + \lambda_{13}e_Z \\ \sigma_Z = \lambda_{13}e_R + \lambda_{13}e_\vartheta + \lambda_{33}e_Z \\ \sigma_{\vartheta Z} = \lambda_{44}e_{\vartheta Z} \\ \sigma_{RZ} = \lambda_{44}e_{RZ} \\ \sigma_{R\vartheta} = (\lambda_{11} - \lambda_{12})e_{R\vartheta} \end{cases} \tag{3}$$

here λ_{ij} is the elastic modulus.

Under axi-symmetric torsion, the displacement components along the R- and Z-axes vanish, and only the circumference displacement $u_\vartheta(R,\vartheta,Z)$ is non-vanishing. In addition, the tubular crack occupies the whole angular range, so the displacement $u_\vartheta(R,\vartheta,Z)$ is asymmetric with respect to ϑ-axis. Because of the assumed symmetry about the ϑ-axis in geometry and the applied loading, the solution of the crack problem is simplified. Assuming that $u_R = u_Z = 0$ and $\partial u_\vartheta/\partial\vartheta = 0$, therefore, the Cauchy Eq. (2) for the present problem can be reduced as

$$e_R = e_Z = e_{RZ} = e_\vartheta = 0; e_{R\vartheta} = \frac{\partial u_\vartheta}{\partial R} - \frac{u_\vartheta}{R}; e_{Z\vartheta} = \frac{\partial u_\vartheta}{\partial Z}. \tag{4}$$

Substituting Eq. (4) into Eq. (3), the corresponding stresses are given by

$$\sigma_R = \sigma_\vartheta = \sigma_Z = \sigma_{RZ} = 0; \sigma_{\vartheta Z} = 2\lambda_{55}e_{\vartheta Z}; \sigma_{R\vartheta} = (\lambda_{11} - \lambda_{12})e_{R\vartheta} \tag{5}$$

Moreover, only the following equilibrium equations is needed to consider

$$\frac{\partial\sigma_{R\vartheta}}{\partial R} + \frac{\partial\sigma_{\vartheta Z}}{\partial Z} + \frac{2\sigma_{R\vartheta}}{R} = \rho\frac{\partial^2 u_\vartheta}{\partial t^2} \tag{6}$$

So, for the present problem, the basic equations of hexagonal crystals cylinder can be expressed by

$$\left.\begin{array}{l} \sigma_{Z\vartheta}^{(j)} = \mu_j e_{Z\vartheta}^{(j)} \\ \sigma_{R\vartheta}^{(j)} = \mu_j e_{R\vartheta}^{(j)} \end{array}\right\}, (j = 1,2) \tag{7}$$

$$\left.\begin{array}{l} e_{R\vartheta}^{(j)} = \frac{\partial u_\vartheta^{(j)}}{\partial R} - \frac{u_\vartheta^{(j)}}{R} \\ e_{Z\vartheta}^{(j)} = \frac{\partial u_\vartheta^{(j)}}{\partial Z} \end{array}\right\}, (j = 1,2) \tag{8}$$

$$\frac{\partial\sigma_{R\vartheta}^{(j)}}{\partial R} + \frac{\partial\sigma_{\vartheta Z}^{(j)}}{\partial Z} + \frac{2\sigma_{R\vartheta}^{(j)}}{R} = \rho\frac{\partial^2 u_\vartheta^{(j)}}{\partial t^2}, (j = 1,2) \tag{9}$$

where the shear modulus μ is defined as $\mu = 2\lambda_{55} = (\lambda_{11} - \lambda_{12})$ for the hexagonal crystals.

Substituting Eqs. (7)–(8) into Eq. (9) yields the governing equations

$$\frac{\partial^2 u_\vartheta^{(j)}}{\partial R^2} + \frac{\partial^2 u_\vartheta^{(j)}}{\partial Z^2} + \frac{1}{R}\frac{\partial u_\vartheta^{(j)}}{\partial R} - \frac{1}{R^2}u_\vartheta^{(j)} = \frac{1}{V_j^2}\frac{\partial^2 u_\vartheta^{(j)}}{\partial t^2}, (j = 1,2) \tag{10}$$

where $V_j = \sqrt{\mu_j/\rho_j}$ is the speed of the elastic shear wave.

For the problem of a crack moving with a constant velocity along the Z-direction, the Galilean transformation can be introduced as

$$r = R, z = Z - vt, \theta = \vartheta \tag{11}$$

where (r,z,θ) is the translating coordinate system attached to the moving crack for reference. In the transformed coordinate system, Eq. (10) becomes independent of the time variable t, and may be written as

$$\frac{\partial^2 u_\theta^{(j)}}{\partial r^2} + k_j^2\frac{\partial^2 u_\theta^{(j)}}{\partial z^2} + \frac{1}{r}\frac{\partial u_\theta^{(j)}}{\partial r} - \frac{1}{r^2}u_\theta^{(j)} = 0, (j = 1,2) \tag{12}$$

where $k_j = \sqrt{1 - v^2/V_j^2}, (j = 1,2)$.

2.2. Boundary conditions

The problem mentioned above should be solved under the proper boundary conditions. In the history of the theoretical studies of crack problems, the boundary conditions at the crack surfaces are assumed as

$$\sigma_{r\theta}^{(1)}(r_1,z) = \sigma_{r\theta}^{(2)}(r_1,z), (0 < z < L) \tag{13}$$

$$\sigma_{r\theta}^{(1)}(r_1,z) = -\sigma_0, (a < z < b) \tag{14}$$

In addition, it is easily found the difference in circumference displacement between the inner and out cylinder should vanish over the regions $(0 < z < a or b < z < L)$, i.e.

$$u_\theta^{(1)}(r_1,z) = u_\theta^{(2)}(r_1,z), (0 < z < a \text{ or } b < z < L) \tag{15}$$

Li and Lee [22] discussed the effect of constraint edges on singular elastic behavior of crack, in which an orthotropic elastic strip with an internal or edge crack is performed and the crack is assumed normal to the edges and subjected to arbitrary anti-plane shear loading. The strip edges are assumed either traction-free or clamped in their work. The solution pointed out stress intensity factors for an internal crack increase when the crack tip is close to the free edge and decrease when the crack tip is close to the clamped edge. In the present work, similarly, four possible cases of mechanical boundary conditions on the inner surface and outer surface of the composition cylinder can be stated below

$$\sigma_{r\theta}^{(1)}(r_0,z) = 0, \sigma_{r\theta}^{(2)}(r_2,z) = 0, (0 < z < L) \tag{16}$$

$$u_\theta^{(1)}(r_0,z) = 0, u_\theta^{(2)}(r_2,z) = 0, (0 < z < L) \tag{17}$$

$$\sigma_{r\theta}^{(1)}(r_0,z) = 0, u_\theta^{(2)}(r_2,z) = 0, (0 < z < L) \tag{18}$$

$$u_\theta^{(1)}(r_0,z) = 0, \sigma_{r\theta}^{(2)}(r_2,z) = 0, (0 < z < L) \tag{19}$$

They correspond respectively to free–free (F–F) edges, clamped–clamped (C–C) edges, free-clamped (F–C) edges, and clamped-free (C–F) edges, as illustrated in Fig. 3. F–F constraint edges are often used. For a composite cylinder with the C–C edges, this situation may be employed to simulate the inner and outer surface of the cylinder are fixed on the corresponding rigid bodies. A hollow composition inclusion embedded on an infinite rigid matrix may be modeled by the composite cylinder with the F–C constraint edges. In addition, the composite cylinder with the C–F constraint edges can be regarded as a model to study a composite cylinder which inner surface is reinforced by a cylindrical rigid fiber.

Besides the above-mentioned boundary conditions, the free boundary conditions are imposed on the upper end and the lower end of the composite cylinder as

$$\sigma_{z\theta}^{(1)}(r,0) = 0, \sigma_{z\theta}^{(2)}(r,0) = 0, (r_0 < r < r_2) \tag{20}$$

$$\sigma_{z\theta}^{(1)}(r,L) = 0, \sigma_{z\theta}^{(2)}(r,L) = 0, (r_0 < r < r_2) \tag{21}$$

3. Fracture analysis

3.1. Cosine integral transform

So, one can assume that the solutions of the mechanical displacements have solutions in the form as

$$u_\theta^{(j)} = \sum_0^\infty F_j(r)\cos(n\gamma z) + H_j(r)\sin(n\gamma z), (j = 1,2), \tag{22}$$

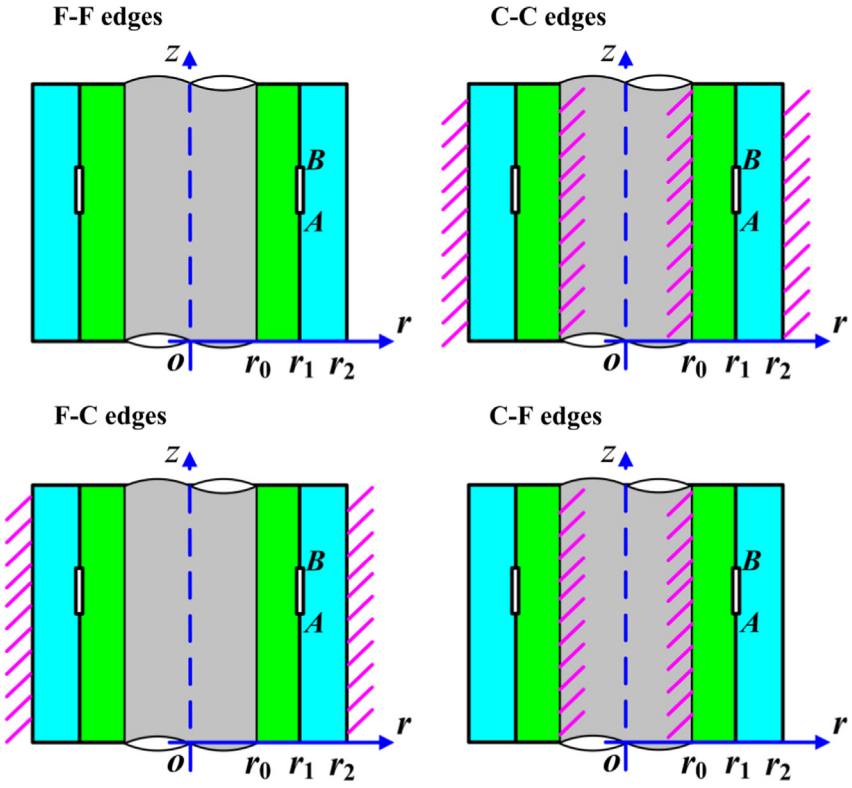

Fig. 3. Schematic of a composition cylinder with a crack for various constraint edges.

where $\gamma=\pi/L$, $F_j(r)$ and $H_j(r),(j=1,2)$ are unknown functions.

Using Eq. (22) can transform the governing equations Eq. (12) into the following ordinary differential equations

$$\begin{cases}\frac{d^2F_j(r)}{d^2r}+\frac{1}{r}\frac{dF_j(r)}{dr}-\left(n^2\gamma^2k_j^2+\frac{1}{r^2}\right)F_j(r)=0,(j=1,2)\\ \frac{d^2H_j(r)}{d^2r}+\frac{1}{r}\frac{dH_j(r)}{dr}-\left(n^2\gamma^2k_j^2+\frac{1}{r^2}\right)H_j(r)=0,(j=1,2)\end{cases} \tag{23}$$

The Eq. (23) is the classical Bessel differential equation, then, solving Eq. (23) yields

$$\begin{cases}F_1(r)=A_nI_1(n\gamma k_1r)+B_nK_1(n\gamma k_1r), & H_1(r)=A_n^*I_1(n\gamma k_1r)+B_n^*K_1(n\gamma k_1r)\\ F_2(r)=C_nI_1(n\gamma k_2r)+D_nK_1(n\gamma k_2r), & H_2(r)=C_n^*I_1(n\gamma k_2r)+D_n^*K_1(n\gamma k_2r)\end{cases} \tag{24}$$

where $A_n, B_n, C_n, D_n, A_n^*, B_n^*, C_n^*$ and D_n^* are unknown coefficients to be determined by boundary conditions, I_k and K_k mean the first and second kinds of modified Bessel functions of the kth order, respectively.

Substituting Eq. (24) into Eq. (22), the solutions of the displacements can be expressed in the form

$$\begin{cases}u_\theta^{(1)}=\sum_{n=0}^{\infty}\left[A_nI_1(n\gamma k_1r)+B_nK_1(n\gamma k_1r)\right]\cos(n\gamma z)+\left[A_n^*I_1(n\gamma k_1r)+B_n^*K_1(n\gamma k_1r)\right]\sin(n\gamma z)\\ u_\theta^{(2)}=\sum_{n=0}^{\infty}\left[C_nI_1(n\gamma k_2r)+D_nK_1(n\gamma k_2r)\right]\cos(n\gamma z)+\left[C_n^*I_1(n\gamma k_2r)+D_n^*K_1(n\gamma k_2r)\right]\sin(n\gamma z)\end{cases} \tag{25}$$

Substituting Eq. (25) into Eqs. (7) and (8), one can obtain the stress expressions of $\sigma_{r\theta}^{(j)}$, $\sigma_{z\theta}^{(j)}$, $(j=1,2)$. Then, it follows from Eqs. (20) and (21) that

$$A_n^*=B_n^*=C_n^*=D_n^*=0 \tag{26}$$

Then, the expressions of $\sigma_{r\theta}^{(j)},(j=1,2)$ can be yielded as

$$\begin{cases}\sigma_{r\theta}^{(1)}=\mu_1\sum_{n=0}^{\infty}\left[A_nG_1(n,r)-B_nG_2(n,r)\right]\cos(n\gamma z)\\ \sigma_{r\theta}^{(2)}=\mu_2\sum_{n=0}^{\infty}\left[C_nG_3(n,r)-D_nG_4(n,r)\right]\cos(n\gamma z)\end{cases} \tag{27}$$

where

$$\begin{cases}G_1(n,r)=n\gamma k_1I_0(n\gamma k_1r)-\frac{2}{r}I_1(n\gamma k_1r)=n\gamma k_1I_2(n\gamma k_1r),\\ G_2(n,r)=n\gamma k_1K_0(n\gamma k_1r)+\frac{2}{r}K_1(n\gamma k_1r)=n\gamma k_1K_2(n\gamma k_1r),\\ G_3(n,r)=n\gamma k_2I_0(n\gamma k_2r)-\frac{2}{r}I_1(n\gamma k_2r)=n\gamma k_2I_2(n\gamma k_2r),\\ G_4(n,r)=n\gamma k_2K_0(n\gamma k_2r)+\frac{2}{r}K_1(n\gamma k_2r)=n\gamma k_2K_2(n\gamma k_2r).\end{cases} \tag{28}$$

3.2. Combined constraint boundary conditions

Based on the orthogonality of the cosine function, substituting Eqs. (25) and (27) into the inner and outer circumferential edges of the composition cylinder which expressed by Eq. (16)–(18), or Eq. (19) gives the following relations

$$B_n=Q_1(n)A_n, D_n=Q_2(n)Q_3(n)A_n\alpha, C=Q_2(n)A_n\alpha. \tag{29}$$

where $\alpha=\mu_1/\mu_2$.

The expressions $Q_1(n), Q_2(n)$ and $Q_3(n)$ in Eq. (29) are different due to the selection of the circumferential edges boundary conditions. The expressions for the F-F edges are given as follows

$$\begin{cases}Q_1(n)=\frac{G_1(n,r_0)}{G_2(n,r_0)},\\ Q_2(n)=\frac{G_4(n,r_2)}{G_2(n,r_0)}\frac{G_1(n,r_1)G_2(n,r_0)-G_1(n,r_0)G_2(n,r_1)}{G_3(n,r_1)G_4(n,r_2)-G_3(n,r_2)G_4(n,r_1)},\\ Q_3(n)=\frac{G_3(n,r_2)}{G_4(n,r_2)}.\end{cases} \tag{30}$$

For the C–C edges, the expressions are obtained as

$$\begin{cases} Q_1(n) = -\frac{I_1(n\gamma k_1 r_0)}{K_1(n\gamma k_1 r_0)}, \\ Q_2(n) = \frac{K_1(n\gamma k_2 r_2)}{K_1(n\gamma k_1 r_0)} \frac{G_1(n,r_1)K_1(n\gamma k_1 r_0)+I_1(n\gamma k_1 r_0)G_2(n,r_1)}{G_3(n,r_1)K_1(n\gamma k_2 r_2)+I_1(n\gamma k_2 r_2)G_4(n,r_1)}, \\ Q_3(n) = -\frac{I_1(n\gamma k_2 r_2)}{K_1(n\gamma k_2 r_2)}. \end{cases} \tag{31}$$

For the F–C edges, the formulae are stated as

$$\begin{cases} Q_1(n) = \frac{G_1(n,r_0)}{G_2(n,r_0)}, \\ Q_2(n) = \frac{K_1(n\gamma k_2 r_2)}{G_2(n,r_0)} \frac{G_1(n,r_1)G_2(n,r_0)-G_1(n,r_0)G_2(n,r_1)}{G_3(n,r_1)K_1(n\gamma k_2 r_2)+I_1(n\gamma k_2 r_2)G_4(n,r_1)}, \\ Q_3(n) = -\frac{I_1(n\gamma k_2 r_2)}{K_1(n\gamma k_2 r_2)}. \end{cases} \tag{32}$$

For the C–F edges, the formulae are expressed as

$$\begin{cases} Q_1(n) = -\frac{I_1(n\gamma k_1 r_0)}{K_1(n\gamma k_1 r_0)}, \\ Q_2(n) = \frac{G_4(n,r_2)}{K_1(n\gamma k_1 r_0)} \frac{G_1(n,r_1)K_1(n\gamma k_1 r_0)+I_1(n\gamma k_1 r_0)G_2(n,r_1)}{G_3(n,r_1)G_4(n,r_2)-G_3(n,r_2)G_4(n,r_1)}, \\ Q_3(n) = \frac{G_3(n,r_2)}{G_4(n,r_2)}. \end{cases} \tag{33}$$

3.3. Transformation to a singular integral equation

One can use the method of Cauchy singular integral equation to obtain the singular behavior for the crack problem. To this end, the following dislocation density function is introduced

$$g(z) = \begin{cases} \frac{d}{dz}[u_\theta^{(1)}(r_1,z) - u_\theta^{(2)}(r_1,z)], & a < z < b \\ 0, & 0 < z < a \quad or \quad b < z < L \end{cases} \tag{34}$$

It follows from Eq. (34) that Eq. (15) is automatically satisfied and the following single-valued condition holds

$$\int_a^b g(z)dz = 0 \tag{35}$$

Substituting Eqs. (25) (26) and (29) into Eq. (34), then, using the orthogonality of sine functions, one can represent the coefficients A by the following integral

$$A_n = \frac{Q_4(n)}{L}\int_a^b g(t)\sin(n\gamma t)\,dt \tag{36}$$

where

$$Q_4(s) = \frac{2}{n\gamma}\frac{1}{\{Q_2(n)\alpha[I_1(n\gamma k_2 r_1)+Q_3(n)K_1(n\gamma k_2 r_1)]-I_1(n\gamma k_1 r_1)-Q_1(n)K_1(n\gamma k_1 r_1)]\}} \tag{37}$$

From Eqs. (27), (29) and (36), one can transform Eq. (14) into an integral equation

$$\frac{2}{L}\int_a^b g(t)\sum_{n=0}^{\infty} Q_5(n)\sin(n\gamma t)\cos(n\gamma z)dt = -\frac{\sigma_0}{\mu_1} \tag{38}$$

where

$$Q_5(n) = Q_4(s)[G_1(n,r) - Q_1(s)G_2(n,r)] \tag{39}$$

When n approaches infinity, the asymptotic value of $Q_5(n)$ is

$$\lim_{n\to\infty} Q_5(n) = q \neq 0 \tag{40}$$

in which q is a constant dependent on the material properties and it can be evaluated numerically during computation.

Because only the asymptotic value of $Q_5(n)$ would lead to singular integral in Eq. (38), by adding and subtracting this asymptotic value to and from $Q_5(n)$, one can obtain an integral equation in the form

$$\frac{2}{L}\int_a^b g(t)\left[-\frac{1}{2}\frac{\sin(\gamma t)}{\cos(\gamma t)-\cos(\gamma z)} - R_0(t,z)\right]dt = -\frac{\sigma_0}{q\mu_1} \tag{41}$$

where

$$R_0(t,z) = \sum_{n=0}^{\infty}\left(1-\frac{Q_5(n)}{q}\right)\sin(n\gamma t)\cos(n\gamma z) \tag{42}$$

In the derivation of Eq. (41), the following identity is employed

$$\sum_{n=0}^{\infty}\sin(n\gamma t)\cos(n\gamma z) = -\frac{1}{2}\frac{\sin(\gamma t)}{\cos(\gamma t)-\cos(\gamma z)} \tag{43}$$

Introducing $t_1 = \cos(\gamma t), z_1 = \cos(\gamma z), a_1 = \cos(\gamma a)$ and $b_1 = \cos(\gamma b)$, one can recast Eq. (41) into a Cauchy singular integral equation

$$\frac{2}{\pi}\int_{a_1}^{b_1} G(t_1)\left[\frac{1}{2}\frac{1}{t_1 - z_1} + R(t_1,z_1)\right]dt_1 = -\frac{\sigma_0}{q\mu_1}, a_1 < z_1 < b_1 \tag{44}$$

where $G(t_1) \equiv g(t), R(t_1,z_1) = R_0(t,z)\csc(\gamma t)$.

Introducing $t_1 = a_0 + c_0\tilde{t}, z_1 = a_0 + c_0\tilde{z}, a_0 = (a_1+b_1/2), c_0 = (b_1 - a_1/2)$, one can obtain the singular integral equation

$$\frac{1}{\pi}\int_{-1}^{1} f(\tilde{t})\left[\frac{1}{\tilde{t}-\tilde{z}} + \tilde{R}(\tilde{t},\tilde{z})\right]d\tilde{t} = -\frac{\sigma_0}{q\mu_1}, \tag{45}$$

where $\tilde{R}(\tilde{t},\tilde{z}) = 2c_0 R(t_1,z_1), f(\tilde{t}) \equiv G(t_1)$.

Here the integral at the left-hand side of (45) is understood in the sense of Cauchy principal value. So the resulting Eq. (45) is a first kind singular integral equation with a Cauchy kernel.

3.4. Solution of the singular integral equation

According to the theory of singular integral equations, the solution of $f(\tilde{t})$ may be expressed by

$$f(\tilde{t}) = \frac{\sigma_0}{q\mu_1}\frac{\psi(\tilde{t})}{\sqrt{1-\tilde{t}^2}} \tag{46}$$

where $\psi(\tilde{t})$ is an unknown dimensionless function being continuous and bounded in the interval of $|\tilde{t}| < 1$ and nonzero at the end points $\tilde{t} = \pm 1$.

Eqs. (35) and (45) are reduced into a system of algebraic equations by the Lobatto–Chebyshev collocation method

$$\begin{cases} \sum_{j=0}^{m}\left[\frac{1}{\tilde{t}_j - \tilde{z}_k} + \tilde{R}(\tilde{t}_j,\tilde{z}_k)\right]\lambda_j\psi(\tilde{t}_j) = -m \\ \sum_{j=0}^{m}\lambda_j\psi(\tilde{t}_j) = 0 \end{cases} \tag{47}$$

where m is the node number of the numerical quadrature. The coefficients $\lambda_0 = \lambda_m = 1/2$ and $\lambda_1 = \ldots = \lambda_{m-1} = 1$, and the discrete values of $\tilde{t}_j, \tilde{z}_k$ are

$$\begin{cases} \tilde{t}_j = \cos(j\pi/m), (j = 0,1,\ldots,m) \\ \tilde{z}_k = \cos[(2k-1)\pi/2m], (k = 1,\ldots,m) \end{cases} \tag{48}$$

Solving Eq. (47), the numerical values of the function $\psi(\tilde{t}_j)$ can be obtained, and then the stress intensity factors (SIFs) can be further determined.

3.5. Formula of stress intensity factor

Due to the symmetry of the problem, only the SIFs of the crack tip A and B are studied here, and they are defined by

$$K_A = \lim_{z\to a^-}\sigma_{r\theta}(r_1,z)\sqrt{2\pi(a-z)}, K_B = \lim_{z\to b^+}\sigma_{r\theta}(r_1,z)\sqrt{2\pi(z-b)} \tag{49}$$

The singular stress at the crack tip is

$$\sigma_{r\theta}(r_1,z)=\frac{q\mu_1}{\pi}\int_{-1}^{1}\frac{f(\tilde{t})}{\tilde{t}-\tilde{z}}d\tilde{t}=\frac{\sigma_0}{\pi}\int_{-1}^{1}\frac{\psi(\tilde{t})}{\sqrt{1-\tilde{t}^2}}\frac{1}{\tilde{t}-\tilde{z}}d\tilde{t} \tag{50}$$

Taking into account the equalities as

$$\frac{1}{\pi}\int_{-1}^{1}\frac{1}{(\tilde{t}-\tilde{z})\sqrt{1-\tilde{t}^2}}d\tilde{t}=\begin{cases}-\frac{1}{\sqrt{\tilde{z}^2-1}}, & \tilde{z}>1\\ 0, & |\tilde{z}|<1\\ \frac{1}{\sqrt{\tilde{z}^2-1}}, & \tilde{z}<-1\end{cases} \tag{51}$$

one can obtain

$$\lim_{z\to a^-}\sigma_{r\theta}(r_1,z)=\sigma_0\frac{\psi(-1)}{\sqrt{\tilde{z}^2-1}},\quad \lim_{z\to b^+}\sigma_{r\theta}(r_1,z)=-\sigma_0\frac{\psi(1)}{\sqrt{\tilde{z}^2-1}} \tag{52}$$

Considering $t_1=\cos(\gamma t)$, $z_1=\cos(\gamma z)$, $a_1=\cos(\gamma a)$, $b_1=\cos(\gamma b)$, $t_1=a_0+c_0\tilde{t}$, $z_1=a_0+c_0\tilde{z}$, $a_0=a_1+b_1/2$ and $c_0=b_1-a_1/2$, and substituting Eq. (52) into Eq. (49), the SIF is obtained as

$$\begin{cases}K_A=\sigma_0\psi(-1)\sqrt{L/2}\sqrt{\frac{\cos(\gamma a)-\cos(\gamma b)}{\sin(\gamma a)}},\\ K_B=-\sigma_0\psi(1)\sqrt{L/2}\sqrt{\frac{\cos(\gamma a)-\cos(\gamma b)}{\sin(\gamma b)}}.\end{cases} \tag{53}$$

Dividing $\sigma_0\sqrt{\pi(b-a)/2}$, the normalized SIF is defined by

$$\begin{cases}K_A^0=\frac{\psi(-1)}{\sqrt{\gamma(b-a)}}\sqrt{\frac{\cos(\gamma a)-\cos(\gamma b)}{\sin(\gamma a)}},\\ K_B^0=-\frac{\psi(1)}{\sqrt{\gamma(b-a)}}\sqrt{\frac{\cos(\gamma a)-\cos(\gamma b)}{\sin(\gamma b)}}.\end{cases} \tag{54}$$

4. Numerical results and discussion

4.1. Numerical verification

Before going into detail discussion, the results of a simple problem degenerated from the present problem will be compared with those of the previous study. Let us consider a center static tubular interface crack in a composite cylinder with F-F edges, which is investigated by Li et al. [9]. The geometric and physical parameters of the present problem can be changed to simulate the crack problem of [9], such as $\nu=0$ and the length L is far greater than the crack length $b-a$. Fig. 4 shows that if $\nu=0$ the present numerical results agree well with those of Li et al. [9] (see Fig. 7 of Li et al. [9]). As a result, the present formulations have been validated.

4.2. Parametric studies

4.2.1. Effects of geometrical parameters

The effect of the thickness ratio on the normalized SIF is shown in Fig. 4 with four typical combined constraint boundary conditions. Clearly, the smaller thickness ratio is, the relatively thinner thickness of the inner cylinder is. So, Fig. 4 shows a noticeable phenomenon that the stress intensity factors for an interface crack increase with the interface approaching to the free edge, and decrease with the interface close to the clamped edge. In addition, the similar phenomenon can also be found from the internal crack problem with various boundary conditions (see Fig. 3 of Li and Lee [22]). There only exist the different boundary conditions on the inner surfaces between the F-F and C–F edges (or C–C and F–C edges), but they have the same boundary conditions on the outer surfaces. So, it is indicated in Fig. 5 that when the thickness ratio tends to a large value, the SIF with the same outer surfaces and different inner surfaces boundary conditions tends to the same value. For similar reasons, Fig. 5 also displays that when the thickness ratio becomes smaller, the SIF with the same inner surfaces and different outer surfaces boundary conditions tends to the same value.

Fig. 6 shows the effect of the crack's location on the normalized SIF K_A^0 and K_B^0 for FF cases. Here, the crack's dimensionless location is expressed by $(a+b)/2L$. As the crack moves near to a radial edge, the SIF of the crack tip pointing to this end tends to infinity as follows from Eq. (54) with $a\to 0$ or $b\to L$, but that of the crack tip pointing to the opposite direction experiences a slight decrease. This kind of increase or decrease in the SIF is referred to as the free

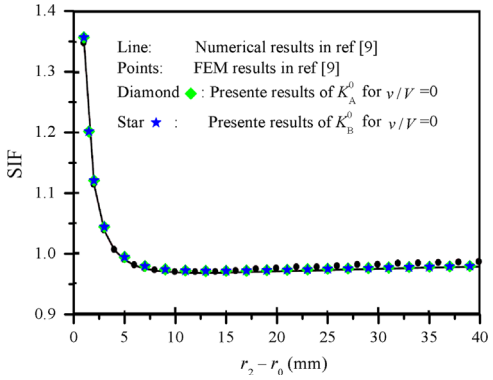

Fig. 4. Comparison between the present numerical results and the results of reference ($r_0=10$ mm; $(r_1-r_0)/(r_2-r_1)=1$; $L=100$ mm; $b+a=L$; $b-a=4$ mm; $\nu=0$.).

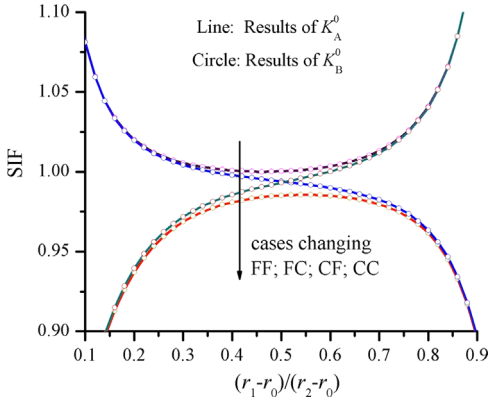

Fig. 5. Variation of the normalized SIF K_A^0 and K_B^0 vs the thickness ratio $r_1-r_0/r_2-r_1(r_0=10$ mm; $r_2=30$ mm; $L=50$ mm; $b+a=L$; $b-a=5$ mm; $\alpha=2$; $\nu/V_1=0.2$.)

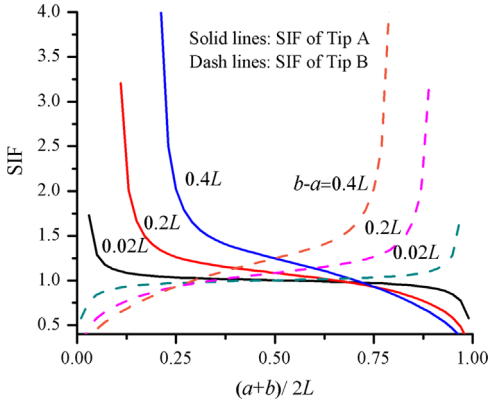

Fig. 6. The normalized SIF K_A^0 and K_B^0 versus the crack location $(a+b)/2$ for FF cases ($r_0=10$ mm; $r_1=24$ mm; $r_2=30$ mm; $L=50$ mm; $\alpha=2$; $\nu/V_1=0.2$.).

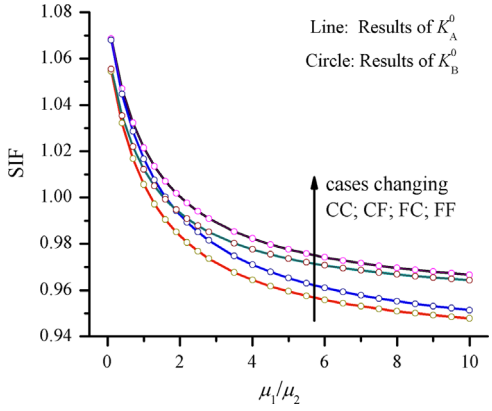

Fig. 7. Variation of the normalized SIF K_A^0 and K_B^0 for the different edges vs the stiffness ratio μ_1/μ_2 ($r_0=20$ mm; $r_1=30$ mm; $r_2=40$ mm; $L=50$ mm; $b+a=L$; $b-a=5$ mm; $v/V=0.2$.).

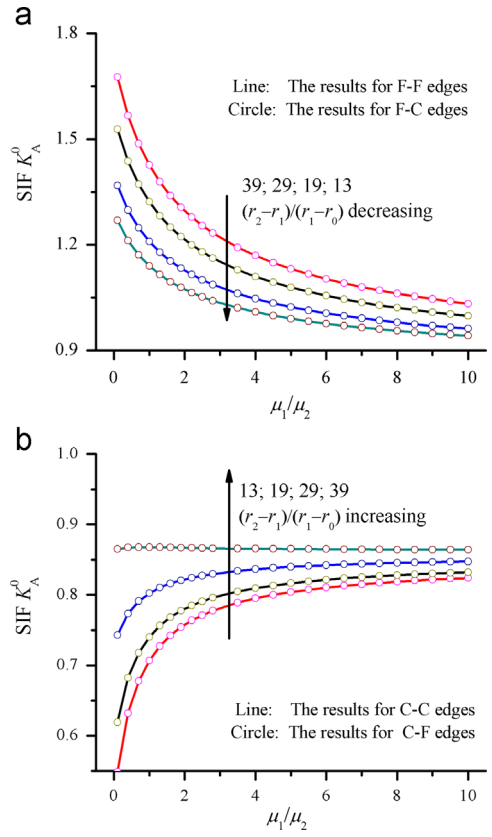

Fig. 8. Variation of the normalized SIF K_A^0 for the different edges vs the stiffness ratio μ_1/μ_2 ($r_0=10$ mm; $r_2=40$ mm; $r_2=40$ mm; $L=50$ mm; $b+a=L$; $b-a=5$ mm; $v/V=0.2$.).

edge effect. In addition, the variations of the SIFs of the two crack tips are symmetrically distributed with respect to the center location of the cylinder. This symmetry of the SIFs comes from the geometrical symmetry and demonstrates the validity of the theoretical derivation and numerical computation. Fig. 5 also shows that the SIFs increase with the crack length $b-a$ increasing. Additionally, it is observed that longer cracks are more sensitive to the free edge effect than the shorter cracks do.

4.2.2. *Effects of stiffness ratio*

When the inner and outer cylinder thickness are equal, with the stiffness ratio μ_1/μ_2 varying from 0.1 to 10.0, Fig. 7 shows that a larger stiffness ratio will produce larger SIF. It is easy to conclude

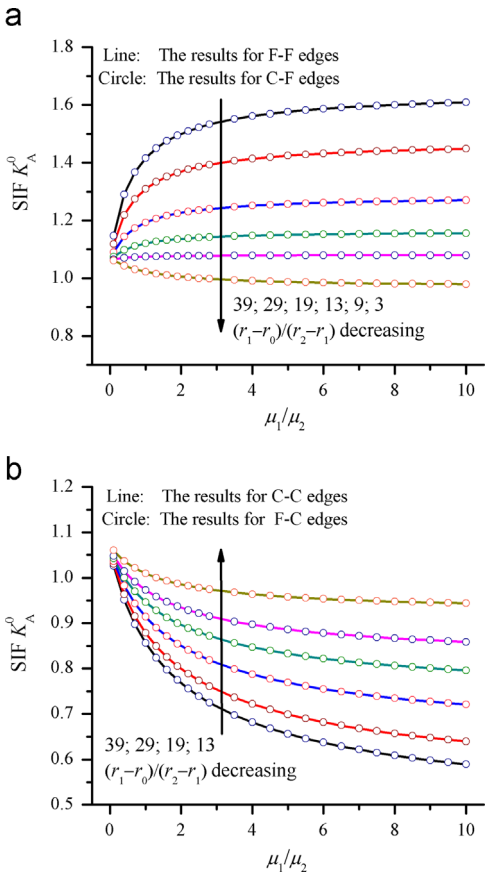

Fig. 9. Variation of the normalized SIF K_A^0 for the different edges vs the stiffness ratio μ_1/μ_2 ($r_0=10$ mm; $r_2=40$ mm; $r_2=40$ mm; $L=50$ mm; $b+a=L$; $b-a=5$ mm; $v/V_1=0.2$.).

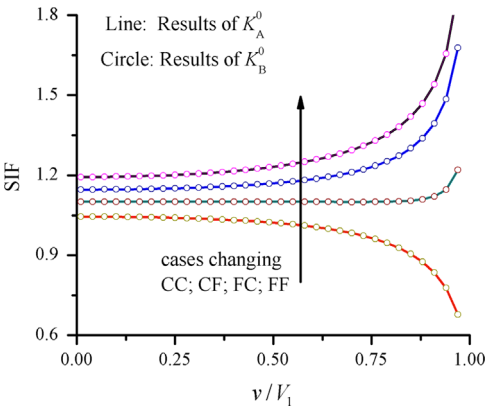

Fig. 10. Variation of the normalized SIF K_A^0 and K_B^0 vs the crack moving velocity v/V_1 ($r_0=20$ mm; $r_1=30$ mm; $r_2=40$ mm; $L=50$ mm; $b+a=L$; $b-a=20$ mm; $\alpha=1.2$.)

that, when the inner and outer cylinder thickness are equal, decreasing the stiffness of the inner elastic substrate or increasing the stiffness of the outer elastic cylinder can help to lower down the SIF of the interface crack. This result is in agreement with the conclusion made for a composition cylindrical structure (see Fig. 8 of Li and Shi [7]).

When the inner and outer radii are given, for the F–F and F–C edges, Fig. 8 shows if the outer cylinder is thick enough (the thickness ratio between the out and inner cylinder is greater than 13), to increase the stiffness ratio also can help to lower down the SIF of the tubular interface crack. For F–F and F–C edges, therefore, a direct method is derived that the possible fracture can be

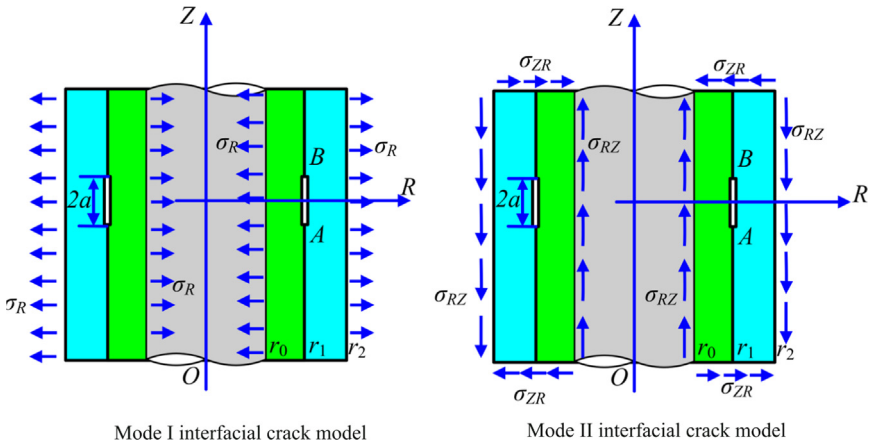

Fig. 11. Model I and model II case for a hollow composite cylinder with a tubular interface crack.

avoided by increasing the stiffness ratio when the outer cylinder is enough thickness. For the C–C and C–F edges, however, if the thickness ratio between out cylinder and inner cylinder is greater than 19, the SIF increase with the addition of the stiffness ratio. So, for C–C and C–F edges, when choosing optimal physical parameters in design, one should take this thickness of outer cylinder into consideration.

When the inner and outer radii are given, Fig. 9 shows when the outer cylinder is thin enough (the thickness ratio between the inner and outer cylinder is greater than 13), a softer inner cylinder plus a stiffer outer cylinder becomes an anti-fracture optimal design for the F–F and C–F edges. But, Fig. 9 also depicts increase the stiffness ratio is beneficial to SIF reduction for the F–F and C–F edges when the thickness ratio between the inner and outer cylinder is less than 13. This indicates that the effects of the geometrical parameters are coupled together with those of the physical parameters. Therefore, to achieve an anti-fracture design, the physical parameters should match the geometrical parameters in magnitude. However, a direct method is derived that one can avoid the possible fracture for C–C and F–C edges by increasing the stiffness ratio when the thickness ratio between the inner and outer cylinder is greater than 3.

4.2.3. *Effects of crack moving velocity*

From Fig. 10, it can be seen that the normalized stress intensity factor increases as the crack moving velocity increases for the free–free, free–clamped, or clamped–free edges. However, for the clamped–clamped edge, the stress intensity factor decreases with the increasing crack moving velocity. Singh and Moodie [23] considered the effect of the various boundaries on the fracture behaviors for the finite length cracks propagating with constant velocity in infinitely long finite width strips. Two boundaries investigated in their work correspond to the F–F edges and C–C edges proposed in the present paper. These present relationships between the crack moving velocity and the stress intensity factors shown in Fig. 10 are in accordance with the previous results obtained by Singh and Moodie [23] (see Figs. 2 and 3 of Singh and Moodie [23]).

5. Simple discussion for other types of interface crack

The interface crack problems of composite materials consist of two parts. One part is familiar and important model I, model II and mixed model of I-II, and the other part is model III. For the model I, model II and mixed model of I-II interfacial crack, an oscillating stress singularity appears in the interface. However, the interfacial

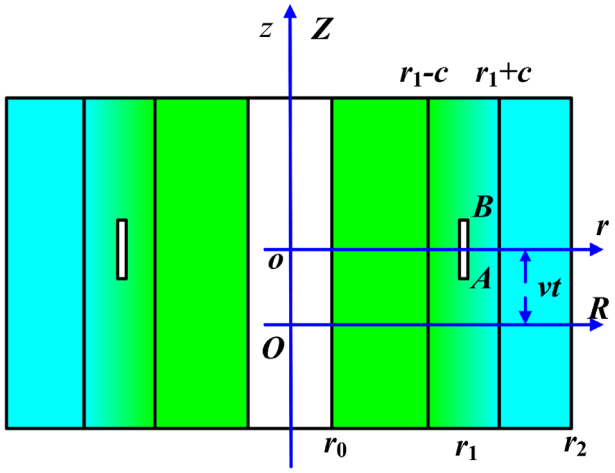

Fig. 12. A continuum region model for the hollow composite cylinder with model I or II interface crack.

crack-tip field for model III cracks manifests the standard square-root singularity [24,25]. In our work above, the cylindrical interface crack can be treated as a model III interface problem in cylindrical coordinate system. So, there are no issues about the exponent of the singularity in this problem. As shown in Fig. 11, if the cylindrical structure is under axial stretch, the cylindrical crack has the nature of mode I when viewed in the axial section. If the cylindrical structure is under axial shear, the cylindrical crack has the nature of mode II when viewed in the axial section. It is known that oscillatory singularities appear in problems involving a model I or model II interface cracks that are assumed to have open tips. An unsatisfactory aspect of the oscillatory singularities is that they lead to overlapping of the crack faces.

The crack advances dynamically in our model. To avoid the oscillatory singularities, for this dynamical case, the interface may be simulated as a very thin continuum region with graded properties. This approach can be traced back to around 20 years ago [26]. As shown in Fig. 12, suppose that two elastic cylinders are perfectly bonded through an elastic graded cylinder. The graded interfacial cylinder has the thickness of $2c$, its material property is assumed to vary as a power form and satisfies the continuity conditions of the material properties at the interfaces $r=r_1-c$ and $r=r_1+c$. Furthermore, one can model the graded interfacial cylinder as piece-wise multi-layered cylinder, that is, to divide the graded interfacial cylinder

into multiple sub-cylinders with constant material properties in the gradient direction. The detailed description can be found in the previous work by S. Itou [27]. The advantage of this approach features avoiding the trouble parts related to the complex governing equations with graded properties.

For Mode I and II interfacial crack problems, only the circumference displacement $u_\vartheta(R,\vartheta,Z)$ is vanishing. In addition, the tubular crack occupies the whole angular range, so the displacement $u_Z(R,\vartheta,Z), u_R(R,\vartheta,Z)$ is asymmetric with respect to the ϑ-axis. Because of the assumed symmetry about the ϑ-axis in geometry and the applied loading, the solution of the crack problem is simplified. Assuming that $u_\vartheta=0$ and $\partial u_R/\partial\vartheta=\partial u_Z/\partial\vartheta=0$, therefore, the Cauchy Eq. (2) for the present problem can be reduced as

$$e_R=\frac{\partial u_R}{\partial R};\ e_\vartheta=\frac{u_R}{R};\ e_Z=\frac{\partial u_Z}{\partial Z};\ e_{RZ}=\frac{\partial u_Z}{\partial R}+\frac{\partial u_R}{\partial Z};\ e_{R\vartheta}=e_{Z\vartheta}=0. \tag{55}$$

Substituting Eq. (55) into Eq. (3), the corresponding stresses are given by

$$\left.\begin{aligned}&\sigma_R=\lambda_{11}\tfrac{\partial u_R}{\partial R}+\lambda_{12}\tfrac{u_R}{R}+\lambda_{13}\tfrac{\partial u_Z}{\partial Z}\\&\sigma_\vartheta=\lambda_{12}\tfrac{\partial u_R}{\partial R}+\lambda_{11}\tfrac{u_R}{R}+\lambda_{13}\tfrac{\partial u_Z}{\partial Z}\\&\sigma_Z=\lambda_{13}\tfrac{\partial u_R}{\partial R}+\lambda_{13}\tfrac{u_R}{R}+\lambda_{33}\tfrac{\partial u_Z}{\partial Z}\\&\sigma_{RZ}=\lambda_{44}\left(\tfrac{\partial u_Z}{\partial R}+\tfrac{\partial u_R}{\partial Z}\right)\\&\sigma_{\vartheta Z}=\sigma_{R\vartheta}=0\end{aligned}\right\} \tag{56}$$

Moreover, only the following equilibrium equations is needed to consider

$$\left.\begin{aligned}&\tfrac{\partial\sigma_R}{\partial R}+\tfrac{\sigma_R-\sigma_\vartheta}{R}+\tfrac{\partial\sigma_{RZ}}{\partial Z}=\rho\tfrac{\partial^2 u_R}{\partial t^2}\\&\tfrac{\partial\sigma_{RZ}}{\partial R}+\tfrac{\sigma_{RZ}}{R}+\tfrac{\partial\sigma_Z}{\partial Z}=\rho\tfrac{\partial^2 u_Z}{\partial t^2}\end{aligned}\right\} \tag{57}$$

Substituting Eq. (56) into Eq. (57) yields the governing equations

$$\left.\begin{aligned}&\lambda_{11}\left(\tfrac{\partial^2 u_R}{\partial R^2}+\tfrac{1}{R}\tfrac{\partial u_R}{\partial R}-\tfrac{u_R}{R^2}\right)+\lambda_{44}\tfrac{\partial^2 u_R}{\partial Z^2}+(\lambda_{13}+\lambda_{44})\tfrac{\partial^2 u_Z}{\partial R\partial Z}=\rho\tfrac{\partial^2 u_R}{\partial t^2}\\&(\lambda_{13}+\lambda_{44})\left(\tfrac{\partial^2 u_R}{\partial R\partial Z}+\tfrac{1}{R}\tfrac{\partial u_R}{\partial Z}\right)+\lambda_{44}\left(\tfrac{\partial^2 u_Z}{\partial R^2}+\tfrac{1}{R}\tfrac{\partial u_Z}{\partial R}\right)+\lambda_{33}\tfrac{\partial^2 u_Z}{\partial Z^2}=\rho\tfrac{\partial^2 u_Z}{\partial t^2}\end{aligned}\right\} \tag{58}$$

For the problem of a crack moving with a constant velocity along the Z-direction, the Galilean transformation Eq. (11) is satisfied. In the transformed coordinate system, Eq. (58) becomes independent of the time variable t, and may be written as

$$\left.\begin{aligned}&\lambda_{11}\left(\tfrac{\partial^2 u_r}{\partial r^2}+\tfrac{1}{r}\tfrac{\partial u_r}{\partial r}-\tfrac{u_r}{r^2}\right)+\lambda_{44}k_1^2\tfrac{\partial^2 u_r}{\partial z^2}+(\lambda_{13}+\lambda_{44})\tfrac{\partial^2 u_z}{\partial r\partial z}=0\\&(\lambda_{13}+\lambda_{44})\left(\tfrac{\partial^2 u_r}{\partial r\partial z}+\tfrac{1}{r}\tfrac{\partial u_r}{\partial z}\right)+\lambda_{44}\left(\tfrac{\partial^2 u_z}{\partial r^2}+\tfrac{1}{r}\tfrac{\partial u_z}{\partial r}\right)+\lambda_{33}k_2^2\tfrac{\partial^2 u_z}{\partial z^2}=0\end{aligned}\right\} \tag{59}$$

where $k_1=\sqrt{1-v^2/V_1{}^2}, k_2=\sqrt{1-v^2/V_2{}^2}, V_1=\sqrt{\lambda_{44}/\rho}, V_2=\sqrt{\lambda_{33}/\rho}$ are the wave velocities.

To determine the analytical general solution of Eq. (59), a generalized displacement potential function $\psi(r,z)$ is introduced by relating it to the displacements u_r and u_z in the following manner [28]:

$$u_r=\frac{\partial\psi}{\partial r}, u_z=p\frac{\partial\psi}{\partial z} \tag{60}$$

where p is a unknown constant to be determined.

The substitution of Eq. (60) into Eq. (59) results in the following governing equations to determine $\psi(r,z)$ and p:

$$\left.\begin{aligned}&\tfrac{\partial}{\partial r}\left\{\lambda_{11}\left(\tfrac{\partial^2\psi}{\partial r^2}+\tfrac{1}{r}\tfrac{\partial\psi}{\partial r}\right)+\left[\lambda_{44}k_1^2+(\lambda_{13}+\lambda_{44})p\right]\tfrac{\partial^2\psi}{\partial z^2}\right\}=0\\&\tfrac{\partial}{\partial z}\left\{(\lambda_{13}+\lambda_{44}+\lambda_{44}p)\left(\tfrac{\partial^2\psi}{\partial r^2}+\tfrac{1}{r}\tfrac{\partial\psi}{\partial r}\right)+\lambda_{33}k_2^2p\tfrac{\partial^2\psi}{\partial z^2}\right\}=0\end{aligned}\right\} \tag{61}$$

Let $\tilde f(r,\xi)$ denotes the Fourier transform of a function $f(r,z)$ with respect to z. Then,

$$\left\{\begin{aligned}&\tilde f(r,\xi)=\tfrac{1}{\sqrt{2\pi}}\int_{-\infty}^{\infty}f(r,z)e^{i\xi z}dz\\&f(r,z)=\tfrac{1}{\sqrt{2\pi}}\int_{-\infty}^{\infty}\tilde f(r,\xi)e^{-i\xi z}d\xi\end{aligned}\right. \tag{62}$$

where ξ denotes the Fourier transform parameter.

Applying Fourier integral transforms to Eq. (61), one obtains the following differential equations in the Fourier transforms domain.

$$\left\{\begin{aligned}&\tfrac{d^2\tilde\psi}{dr^2}+\tfrac{1}{r}\tfrac{d\tilde\psi}{dr}-\tfrac{\lambda_{44}k_1^2+(\lambda_{13}+\lambda_{44})p}{\lambda_{11}}\xi^2\tilde\psi=0\\&\tfrac{d^2\tilde\psi}{dr^2}+\tfrac{1}{r}\tfrac{d\tilde\psi}{dr}-\tfrac{\lambda_{33}pk_2^2}{\lambda_{13}+\lambda_{44}+\lambda_{44}p}\xi^2\tilde\psi=0\end{aligned}\right. \tag{63}$$

Solving the differential equations, the general solutions are obtained in the Fourier transforms domain.

$$\tilde\psi(r,\xi)=\sum_{j=1}^{2}\left[I_0\left(\xi_j r\right)A_j(\xi)+K_0\left(\xi_j r\right)B_j(\xi)\right] \tag{64}$$

where $\xi_j=|\xi|\sqrt{\hbar_j}$, $\hbar_j=(\lambda_{44}k_1^2+(\lambda_{13}+\lambda_{44})p_j/\lambda_{11})$, p_j are a set of roots of the characteristic equation corresponding to Eq. (63) as defined in the following equations

$$\begin{aligned}&(\lambda_{13}+\lambda_{44})\lambda_{44}p^2+\left(\lambda_{13}^2+\lambda_{44}^2+2\lambda_{13}\lambda_{44}+\lambda_{44}^2k_1^2-\lambda_{11}\lambda_{33}k_2^2\right)p\\&\quad+\lambda_{44}(\lambda_{13}+\lambda_{44})k_1^2=0\end{aligned} \tag{65}$$

Therefore, applying Fourier integral transforms and using Eqs. (56) and (64), we can obtain the expansions of the displacement and stresses fields. Based on these general solutions of the displacement and stresses fields and some appropriate boundary conditions, the model I and model II tubular interface crack for a hollow composite cylinder can be solved by using the singular integral equation method and displacement discontinuity technique. The similar detailed procedure for these kinds of crack problems can be found in Refs. [27,29,30] and will not be repeated here.

It should be noted that the methodology used in this manuscript can be extended to plane interface crack problems, but theoretical and computational processes become even more complex. In order to solve the plane interface crack problems by singular integral equation theory, we need to apply the continuum region model and the piece-wise multi-layered cylinder techniques to overcome the difficulties related to stress oscillation and interface penetration existing in Mode I and II interfacial crack problems. The interfacial crack problems are considered in our work. Besides, we should also pay attention to the internal cracks affected by the composite interface, such as the Zener-Stroh crack perpendicular or parallel to the interface [31] and a radial crack in the vicinity of discontinuous interface of the inner and outer cylinders [32].

6. Conclusions

We have considered the problem of Yoffe-type moving crack on the tubular interface in a composite cylinder in this paper. The cylinder is assumed to be under an axi-symmetric torsion with four typical combined constraint boundary conditions. This problem is helpful for understanding the crack propagation in a composite cylinder. The crack is simulated as a continuously distributed dislocation, and then, the singular integral equation method is utilized to solve this problem. Numerical results of the stress intensity factors obtained in the present study are in agreement with the previous work for the static crack with the F–F edges [9] when the crack moving velocity is negligible and the

the cylindrical length is far greater than the crack size. Numerical results of the SIFs are used to survey the effects of geometrical and physical parameters on the stress intensity factors. Summarizing these results as follows: (a) the normalized SIF increases with the crack length increasing; (b) the normalized SIF increases as the crack moving velocity increases for the free -free, free-clamped, or clamped-free edges, and that decreases with the increasing crack moving velocity for the clamped-clamped edge; (c) the coupled effect of geometrical and physical parameters on the interfacial fracture behavior is clearly relates to the selection of constraint edges; (d) as the crack moves near to a radial edge, the SIFs of the crack tip pointing to this end tends to infinity, but that of the crack tip pointing to the opposite direction experiences a slight decrease; (e) SIFs for an interface crack increase with the interface approaching to the free surface, and decrease with the interface close to the clamped surface. The latter two phenomenons are caused by the free boundary effect.

Acknowledgment

This research was supported by a grant of the Fund of the National Natural Science Foundation of China (Nos. 11472201), the Fundamental Research Funds for the Central Universities (No. JB142001-2), and the Open Research Fund of Key Laboratory of Mechanics on Disaster and Environment in Western China (No. Klmwde201406). The authors would wish to express their sincere appreciation to these supports.

References

[1] Vinson JR, Sierakowski RL. The behavior of structures composed of composite materials, vol. 105. Springer; 2006.
[2] Zheng M, Gao C-F. An arc-shaped crack in an electrostrictive material. Int J Eng Sci 2010;48(9):771–82.
[3] Feng FX, Lee KY, Li YD. Multiple cracks on the arc-shaped interface in a semi-cylindrical magneto-electro-elastic composite with an orthotropic substrate. Eng Fract Mech 2011;78(9):2029–41.
[4] Fan M, Yi DK, Xiao ZM. An interfacial arc-shaped Zener–Stroh crack due to inclusion–matrix debonding in composites. Acta Mech 2013:1–10.
[5] Shi PP, Sun S, Li X. Arc-shaped interfacial crack in a non-homogeneous electro-elastic hollow cylinder with orthotropic dielectric layer. Meccanica 2013;48(2):415–26.
[6] Shi PP, Sun S, Li X. The cyclically symmetric cracks on the arc-shaped interface between a functionally graded magneto-electro-elastic layer and an orthotropic elastic substrate under static anti-plane shear load. Eng Fract Mech 2013;105(1):415–26.
[7] Li X, Shi PP. The cyclically symmetric anti-plane fracture analysis for the arc-shaped interface in a non-homogeneous bimaterial cylindrical structure. Acta Mech 2014;225(3):893–907.
[8] Fan M, Yi DK, Xiao ZM. Elastic–plastic stress investigation for an arc-shaped interface crack in composite material. Int J Mech Sci 2014;83:104–11.
[9] Li YD, Zhao H, Xiong T. The cylindrical interface crack in a layered tubular composite of finite thickness under torsion. Eur J Mech A-Solid 2013;39:113–9.
[10] Wang YS, Wang D. Scattering of elastic waves by a rigid cylindrical inclusion partially debonded from its surrounding matrix—I. SH case. Int J Solids Struct 1996;33(19):2789–815.
[11] Wang XY, Yu SW. Scattering of SH waves by an arc-shaped crack between a cylindrical piezoelectric inclusion and matrix-II: far fields. Int J Fract 2000;100(4):35–40.
[12] Feng WJ, Su RKL, Liu YQ. Scattering of SH waves by an arc-shaped interface crack between a cylindrical magneto-electro-elastic inclusion and matrix with the symmetry of 6 mm. Acta Mech 2006;183(1):81–102.
[13] Yoffe EH. LXXV. The moving griffith crack. Lond Edinb Dublin Philos Mag J Sci 1951;42(330):739–50.
[14] Jin B, Zhong Z. A moving mode-III crack in functionally graded piezoelectric material: permeable problem. Mech Res Commun 2002;29(4):217–24.
[15] Li CY, Weng GJ. Yoffe–type moving crack in a functionally graded piezoelectric material. Proc R Soc Lond A: Math Phys 2002;458:381–99.
[16] Kwon SM. On the dynamic propagation of an anti-plane shear crack in a functionally graded piezoelectric strip. Acta Mech 2004;167(1):73–89.
[17] Hu KQ, Kang YL, Qin QH. A moving crack in a rectangular magnetoelectroelastic body. Eng Fract Mech 2007;74(5):751–70.
[18] Yan Z, Jiang LY. Study of a propagating finite crack in functionally graded piezoelectric materials considering dielectric medium effect. Int J Solids Struct 2009;46(6):1362–72.
[19] Shin JW, Lee YS. A moving interface crack between two dissimilar functionally graded piezoelectric layers under electromechanical loading. Int J Solids Struct 2010;47(20):2706–13.
[20] Hu KQ, Chen ZT, Zhong Z. Pre-kinking analysis of a constant moving crack in a magnetoelectroelastic strip under in-plane loading. Eur J Mech A/Solid 2014;43:25–43.
[21] Grigorenko AY, Loza IA. Shul'Ga NA: Propagation of nonaxisymmetric acousto-electric waves in a hollow cylinder. Int Appl Mech 1984;20(6):517–21.
[22] Li XF, Lee KY. Closed-form solution for an orthotropic elastic strip with a crack perpendicular to the edges under arbitrary anti-plane shear. Z Angew Math Mech 2009;89(5):370–82.
[23] Singh BM, Moodie TB. Closed-form solutions for finite length crack moving in a strip under anti-plane shear stress. Acta Mech 1981;38(1):99–109.
[24] Williams ML. The stresses around a fault or crack in dissimilar media. Bull Seismol Soc Am 1959;49(2):199–204.
[25] Rice JR. Elastic fracture concepts for interfacial crack. J Appl Mech-T ASME 1988;55(3):98–103.
[26] Delale F, Erdogan F. On the mechanical modeling of the interfacial region in bonded half-planes. J Appl Mech-T ASME 1988;55(2):317–24.
[27] Itou S. Stress intensity factors for a moving cylindrical crack in a nonhomogeneous cylindrical layer in composite materials. Arch Appl Mech 2005;75(1):18–30.
[28] Sapsathiarn Y, Senjuntichai T, Rajapakse R. Electro-mechanical load transfer from a fiber in a 1–3 piezocomposite with an imperfect interface. Compos Part B: Eng 2008;39(7):1114–24.
[29] Sapsathiarn Y, Senjuntichai T, Rajapakse R. Cylindrical interface cracks in 1–3 piezocomposites. Compos Part B: Eng 2012;43(5):2257–64.
[30] Kasano H, Matsumoto H, Nakahara. A cylindrical interface crack in a non-homogeneous anisotropic elastic body. Bull JSME 1986;29(253):1973–81.
[31] Fan H, Xiao ZM. A Zener-Stroh crack near an interface. Int J Solids Struct 1997;34(22):2829–42.
[32] Xiao ZM, Bai J. On piezoelectric inhomogeneity related problems—part II: a circular piezoelectric inhomogeneity interacting with a nearby crack. Int J Eng Sci 1999;37(8):961–76.